ORIGINAL PAPER

Characterization of Plasma Polymerized Hexamethyldisiloxane Films Prepared by Arc Discharge

Algirdas Lazauskas · Jonas Baltrusaitis · Viktoras Grigaliūnas · Dalius Jucius · Asta Guobienė · Igoris Prosyčevas · Pranas Narmontas

Abstract Herein, we present a simple method for fabricating plasma polymerized hexamethyldisiloxane films (pp-HMDSO) possessing superhydrophobic characteristics via arc discharge. The pp-HMDSO films were deposited on a soda–lime–silica float glass using HMDSO monomer vapor as a precursor. A detailed surface characterization was performed using scanning electron microscopy and atomic force microscopy. The growth process of the pp-HMDSO films was investigated as a function of deposition time from 30 to 300 s. The non-wetting characteristics of the pp-HMDSO films were evaluated by means of contact angle (CA) measurements and correlated with the morphological characteristics, as obtained from microscopy measurements. The deposited films were found to be nano-structured and exhibited dual-scale roughness with the static CA values close to 170°. Fourier transform infrared spectroscopy analysis was carried out to investigate chemical and functional properties of these films. Methyl groups were identified spectroscopically to

A. Lazauskas (✉) · V. Grigaliūnas · D. Jucius · A. Guobienė · I. Prosyčevas · P. Narmontas
Institute of Materials Science, Kaunas University of Technology, Savanorių av. 271, 50131 Kaunas, Lithuania
e-mail: Algirdas.LAZAUSKAS@stud.ktu.lt

V. Grigaliūnas
e-mail: Viktoras.GRIGALIUNAS@ktu.lt

D. Jucius
e-mail: Dalius.JUCIUS@ktu.lt

A. Guobienė
e-mail: Asta.GUOBIENE@ktu.lt

I. Prosyčevas
e-mail: igorpros@mail.ru

P. Narmontas
e-mail: Pranas.NARMONTAS@ktu.lt

J. Baltrusaitis
PhotoCatalytic Synthesis Group, Faculty of Science and Technology, MESA+ Institute, University of Twente, Meander 229, P.O. Box 217, 7500 AE Enschede, The Netherlands
e-mail: j.baltrusaitis@utwente.nl

be present within the pp-HMDSO films and were proposed to result in the low surface energy of material. The synergy between the dual-scale roughness and low surface energy resulted in the superhydrophobic characteristics of the pp-HMDSO films. A possible mechanism for the pp-HMDSO film formation is proposed.

Introduction

Organosilicon compounds are widely used as precursors in thin film technology. Among them, hexamethyldisiloxane (HMDSO) has gained increasing interest in the last decade due to its ability to form thin films with diverse physicochemical properties. It has been previously shown that HMDSO can be successfully used for synthesis of SiO_x containing amorphous hydrogenated carbon (a-C:H/SiO_x) films with tunable functionality [1, 2]. a-C:H/SiO_x films aside, much attention has been devoted to the synthesis and characterization of plasma polymerized HMDSO films (pp-HMDSO), as they have lower cost and higher deposition rates, when compared to those formed from other organosilicon compounds [3]. The pp-HMDSO films are produced via HMDSO monomers undergoing fragmentation during the deposition process. The resulting pp-HMDSO films often contain not only the functional groups of the HMDSO monomer but also new chemical bonds, thus differing in stoichiometry from that of the monomer. The main factors which contribute to the different HMDSO monomer fragmentation mechanisms and, thus, the structure and properties of the resulting pp-HMDSO films, involve the selection of the plasma excitation method, plasma composition and other deposition parameters, such as gas composition, power density. Depending on their obtained properties, pp-HMDSO films deposited, could find applications in medical field due to their biocompatibility [4, 5], packaging as food containers oxygen-barrier coatings [6], microelectronics as protective films against corrosion [7] and sensing as humidity sensitive layers [8]. Specifically, Aumaille et al. [9] demonstrated that pure HMDSO plasma could provide excellent polymerized barrier films due to the monomer fragmentation with formation of Si–H bonds, which act as hydrophobic water repellents [10]. Importantly, the use of pure HMDSO plasma led to a low monomer fragmentation regime and carbon rich films with the retention of methyl groups were obtained [11], which significantly contributed to their hydrophobic characteristics. Purely HMDSO plasma-based films can be proposed to simplify the deposition process due to the use of a single precursor source. If excellent non-wetting property pp-HMDSO films can be obtained, they could find a widespread application ranging from microelectronics to the industrial applications. For this purpose, pp-HMDSO films should be studied in detail with a focus on their structure–property relationship with emphasis on their surface morphology and wetting properties.

   In this paper, we present a simple method for fabricating superhydrophobic pp-HMDSO films via arc discharge. The pp-HMDSO films were deposited on a soda–lime–silica float glass using only HMDSO monomer vapor as a precursor. A detailed surface characterization was conducted by means of scanning electron microscopy (SEM) and atomic force microscopy (AFM). The growth process of the pp-HMDSO films was investigated by varying the deposition time from 30 to 300 s. The non-wetting characteristics of the pp-HMDSO films were evaluated using contact angle (CA) measurements and these were

correlated with the corresponding morphological characteristics. Fourier transform infrared spectroscopy (FTIR) analysis was carried out to investigate chemical and functional properties of these films.

Experimental Technique

Synthesis of pp-HMDSO Films

A schematic of the experimental set-up used in this study is shown in Fig. 1. The polymethylmetacrylate discharge chamber was of the cylindrical geometry of 70 mm in diameter and 70 mm in height. A rod-shaped graphite anode and cathode, 3 mm in diameter, were placed at the centre of the chamber. The distance between the anode and cathode was 25 mm. A small quartz cuvette containing 0.3 ml of HMDSO solution was put at 20 mm from the anode. Commercially available soda–lime–silica float glass (Pilkington NSG Group Flat Glass Business) of 1 mm thickness was used in this study as a substrate. Glass was cut into 1.5×1.5 cm^2 slides. The substrates were virtually free from any macroscopic surface defects, which otherwise could alter interpretation of our obtained results. Surface preparation method included RCA-1 cleaning. For quality testing of the uncoated glass slide surface hydrophilic properties, contact angle measurements were performed and details described below. Uncoated glass surface exhibited low contact angles ranging from 5° to 7°. Details of the characteristic surface morphology of the soda–lime–silica float glass substrate can be found elsewhere [12]. The substrate was placed at the distance of 15 mm from the electrodes. The chamber was connected to a vacuum line backed by the rotary pump. The deposition was performed at a vacuum of 1×10^{-3} Pa. Arc plasma was generated between anode and cathode using a DC transferred arc process using ~ 4.3 mA current and ~ 25 kV voltage. During the experiment, a white colored material was observed adhering to the surface of the substrate. The selected deposition times of pp-HMDSO films were 30, 60, 180 and 300 s.

Characterization

AFM experiments were carried out in air at room temperature (23 °C) using a Micro-testmachines NT-206 atomic force microscope. AFM data was analyzed using SurfaceXplorer scanning probe microscopy data processing software. Topographical images

Fig. 1 Schematics of basic experimental setup for the arc-discharge technique of pp-HMDSO film deposition
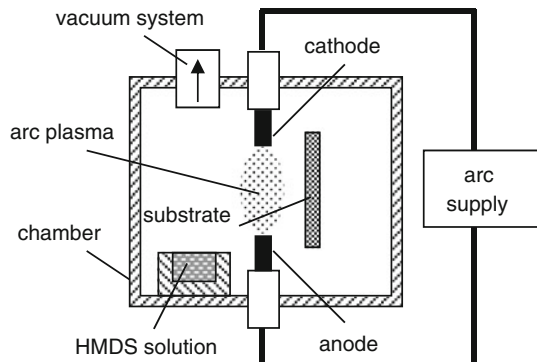
were collected using a V-shaped silicon cantilever (spring constant of 3 N/m, tip curvature radius less than 10.0 nm, full tip cone angle less than 40° and resonance frequency of ~ 65 kHz) operating in the intermittent contact mode.

The surface morphology of the resulting films was evaluated based on the AFM surface topography images, height distribution histograms, bearing ratio curves and roughness parameters, including the root mean square roughness (R_q), skewness (R_{sk}) and kurtosis (R_{ku}). The R_q is the average of the measured height deviations taken within the evaluation area and measured from the mean linear surface. The skewness parameter indicates the symmetry of the surface within the evaluation area. A negative R_{sk} indicates a predominance of valleys while a positive R_{sk} value indicates a surface dominated by peaks. Kurtosis is a measure of the height randomness and sharpness of a surface. For a Gaussian-like surface, R_{ku} it has a value of 3. The farther R_{ku} is from 3, the less random and more repetitive is the surface. The height distribution histogram shows the share of surface points located at a given height relative to the total number of surface points in percent. The bearing ratio curve is defined as the dependence of solid material occurrence on feature height. To obtain more detailed information about surface morphology, hybrid parameters were also characterized by dividing the bearing ratio curve into three regions [13]. The upper region of the bearing ratio curve indicates the portion of surface structures (i.e. peaks), which would primarily be affected during the contact with another surface and is defined as the reduced peak height (R_{pk}). The middle region of the bearing ratio curve indicates the portion of surface structures responsible for stiffness characteristics, performance and life of the surface during wear and is defined as the core-roughness (R_k). The lower region of the bearing ratio curve exhibits surface structures (i.e. valleys) where water molecules adsorbed from the atmosphere could condense or air gabs between contacting surfaces could emerge influencing surface adhesive properties as well as frictional performance and is defined as the reduced valley depth (R_{vk}). Partially masked substrates were used for the pp-HMDSO film thickness evaluation. AFM profiles were collected across non-coat to coat area. The average value of three step heights measured at different positions was used to calculate film thickness.

CA measurements were performed at room temperature (23 °C) using the sessile drop method. One droplet of deionized water (≈ 2 μl) was deposited onto the pp-HMDSO surface. Optical images of the droplet was obtained and CA measured using a method based on B-spline snakes (active contours) [14]. Measurements of the contact angles were taken within 10 s after the formation of each sessile droplet. The average value of five measurements at different positions on the pp-HMDSO surface was used as the static CA (θ_s). However, it is well known, that θ_s alone does not adequately describe the wetting properties of the surface [15]. Therefore, we have used the methodology of Zhang et al. [16] to relate the pp-HMDSO film surface micro- and nanostructure with the measured θ_s to estimate the equilibrium apparent CA (θ_e) and the corresponding contact angle hysteresis (CAH). θ_e may be defined as the θ_s when the droplet is in the stable state of the global free energy minimum on superhydrophobic surfaces, which varies for different surface materials or structural features. CAH is defined as the difference between the CA at the front of the droplet (advancing CA) and at the back of the droplet (receding CA). Namely, CAH occurs due to the surface roughness, microscopic chemical heterogeneity, drop size effect, molecular reorientation, and the penetration of the liquid molecules into the solid surface [17, 18]. In order to compute the above mentioned parameters, a solid fraction (f_s) of the surface micro- and nanostructures, in contact with water droplet, should be known. For this reason, AFM (scan size 40.0 μm × 40.0 μm) and reconstructed SEM (scan size 2.0 μm × 2.0 μm) topographical images were filtered to display the surface micro- and nanostructures which fall into the R_{pk} region (denoted as R_{fs}). Next, the solid fraction of these structures was calculated. The product of the solid fraction of micro- (f_{1s}) and nanostructures (f_{2s}) was attributed to f_s. The θ_e and CAH were determined for the composite wetting state from Eqs. (1) and (2)

$$\theta_e = \arccos[(1 + \cos\theta_s) \cdot f_s - 1] \tag{1}$$

$$CAH = 2 \cdot \left[\arctan\left[1.15 \cdot \left(\sqrt{\frac{2 - (1 + \cos\theta_s) \cdot f_s}{(1 + \cos\theta_s) \cdot f_s}} \right) \right] \right.$$
$$\left. -\arctan\left[0.89 \cdot \left(\sqrt{\frac{2 - (1 + \cos\theta_s) \cdot f_s}{(1 + \cos\theta_s) \cdot f_s}} \right) \right] \right] \tag{2}$$

The composite wetting state was selected as it is mostly associated with the superhydrophobic properties. In this state, the water droplet is partially in contact with air which leads to the sliding up of the droplet or increased droplet mobility [19].

For the experimental evaluation of CAH, advancing and receding CA on the tilted plate was determined. One droplet of deionized water (≈ 5 μl) was carefully placed onto the pp-HMDSO surface, which was then inclined until the droplet started to roll. Image of the water droplet was taken before its motion and advancing and receding CA measured. The average value of five measurements was used. The difference between the advancing and receding CA was adopted as the experimental CAH (CAH$_{exp}$).

FTIR measurements were carried out for the chemical characterization of pp-HMDSO films. A Vertex 70 FT-IR spectrometer (Bruker Optics Inc.) equipped with a 30Spec (Pike Technologies) specular reflectance accessory having a fixed 30° angle of incidence (3/16″ sampling area mask) was used in this study. The spectrum was recorded in the range of 400–4,000 cm^{-1} at a resolution of 4 cm^{-1}. Software OPUS 6.0 (Bruker Optics Inc.) was used for data processing of the baseline-corrected spectra.

X-ray powder diffractometer Dron-3 was used to analyze the structural properties of pp-HMDSO powder collected from a series of deposition processes. Acquisition conditions were 35 kV and 30 mA. Scans were obtained in 2θ diffraction angle between 20° and 70° using Cu-Kα radiation. The XRD pattern (not shown) indicated that the pp-HMDSO consists of the amorphous substances. It can be assumed that the temperature generated by arc plasma was relatively low and HMDSO monomer fragments did not have reactivity to crystallize, which resulted in the non-crystalline structure.

SEM micrographs of the pp-HMDSO films were obtained employing FEI Quanta 200 FEG microscope. The samples were imaged at the accelerating voltage of 30 kV. No coating deposition or any other type of preparation was performed before SEM imaging.

To provide further insights into the pp-HMDSO film formation mechanism, image of the arc discharge generated HMDSO plasma emission between the anode and the cathode was captured. The image was converted to greyscale and brightness and contrast levels were equalized. The luminance of each pixel in the captured image was then interpreted as the intensity for the plot displayed in a thermal lookup table (LUT) scheme for more comprehensive plasma emission interpretation.

Results and Discussion

Surface Morphology and the Corresponding Wetting Properties

AFM topographical images with their corresponding height distribution histograms and bearing ratio curves, as well as SEM images of the resulting pp-HMDSO film surface for deposition time of 30, 60, 180 and 300 s, respectively, are presented in Fig. 2a–d. The pp-HMDSO film thickness of 236, 347, 821 and 1,372 nm was determined for the
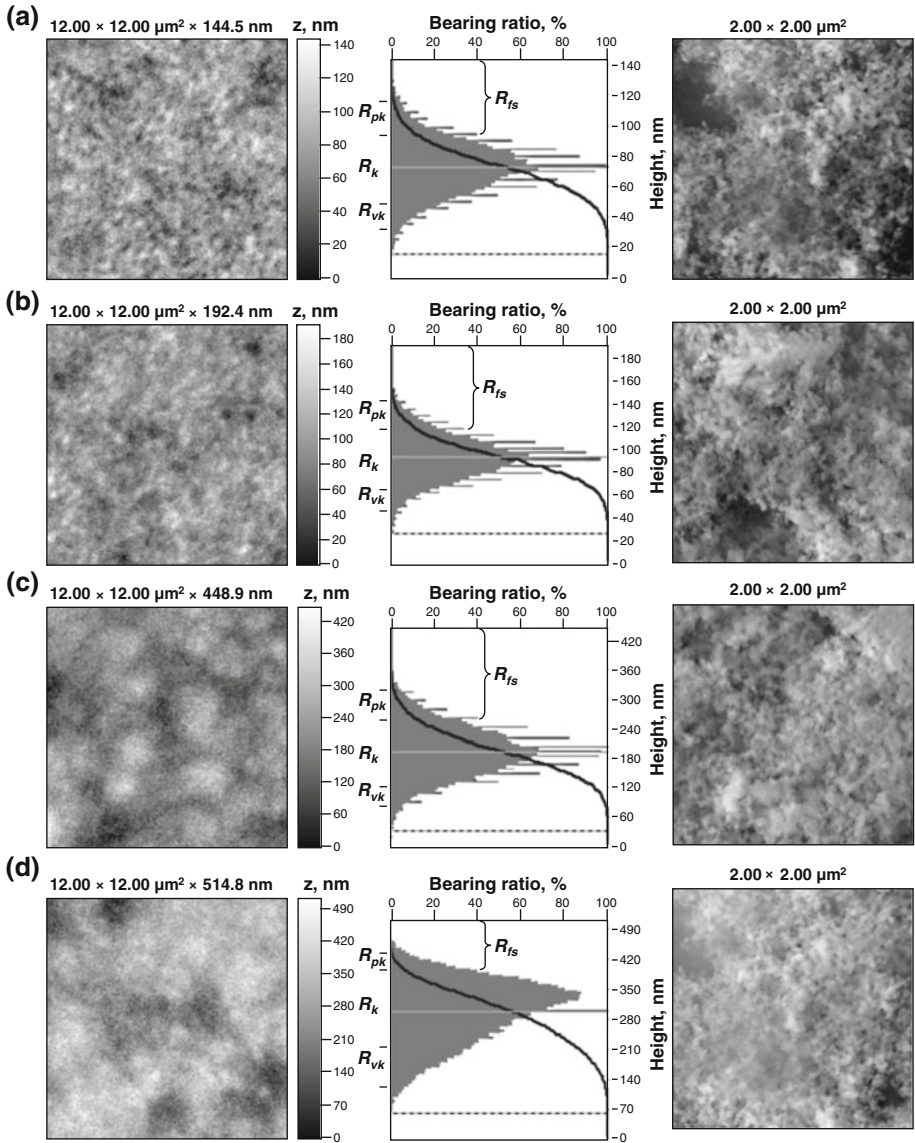
Fig. 2 *Left* AFM characteristic topographical images with normalized Z, nm scale of pp-HMDSO film surface for deposition time of **a** 30 s, **b** 60 s, **c** 180 and **d** 300 s with corresponding (*middle*) normalized height distribution histograms and bearing ratio curves with hybrid parameters indicated, respectively. *Dashed line* indicates the height at which surface structures are connected to each other. The *middle line* indicates the mean height. *Right* SEM images of the resulting pp-HMDSO film surface for selected deposition time

corresponding deposition time. AFM topography images show pp-HMDSO film surfaces composed of the randomly distributed island-like morphological features (Fig. 2a, b, left), which grow in three dimensions and interconnect to form larger aggregates (Fig. 2c, left), as the deposition time increases. The observed film formation is in a good agreement with

Table 1 Summary of surface morphology parameters

Deposition time (s)	Parameters					
	R_q (nm)	R_{sk}	R_{ku}	R_{pk} (nm)	R_k (nm)	R_{vk} (nm)
30	18.03	0.01	3.26	23.93	46.19	22.19
60	20.58	0.09	3.71	25.74	55.00	19.86
180	53.88	0.19	3.40	62.08	143.00	40.44
300	74.06	−0.48	2.82	39.60	185.79	88.32

Volmer-Weber growth mode, suggesting that HMDSO fragments in the deposit are more strongly bound to each other than to the glass substrate [20]. Six statistical parameters, R_q, R_{sk}, R_{ku}, R_{pk}, R_k and R_{vk}, were calculated for each surface (Table 1). The R_q increased as the deposition time increased. A positive R_{sk} value was calculated for pp-HMDSO film surface for deposition time of 30, 60 and 180 s, respectively, indicating a regime where surface peaks dominate the valleys. These surfaces exhibited leptokurtoic [21] distribution of their morphological features having considerable fraction of high peaks and low valleys with R_{ku} value of 3.26, 3.71 and 3.40. However, in contrast to those observed for deposition times of 30, 60 and 180 s, roughness parameters of pp-HMDSO film surface observed for deposition time of 300 s contained some important differences. The surface exhibited negative R_{sk} value of -0.48 indicating a regime where surface valleys dominate the peaks. Also, the leptokurtoic distribution of the morphological features has shifted to platykurtoic distribution indicating a relatively few high peaks and low valleys with R_{ku} value of 2.82. Longer deposition time has led to the interconnection of larger island-like morphological features (Fig. 2d, left) with the formation of a bumpy surface topography. Values of R_{pk}, R_k and R_{vk} (Table 1) derived from the bearing ratio curves (Fig. 2a–d, middle) correlate well with those of R_q, R_{sk}, R_{ku}. Furthermore, when comparing the ratio of R_{pk}/R_k and R_{vk}/R_k qualitative spatial structure information could be obtained. Specifically, R_{pk}/R_k values of 0.52, 0.47, 0.43 and 0.21 were calculated for pp-HMDSO film surface for deposition times of 30, 60, 180 and 300 s, respectively. These data indicate that the highest density of surface peaks in AFM scan area was obtained for the deposition time of 30 s, which is in a good agreement with the AFM topographical images. Any increase in R_{pk} can weaken the mechanical properties of the film as the surface structures, which fall into R_{pk} region, would primarily be affected during the contact with another surface [12]. However, higher R_{pk} value may improve the non-wetting properties of the film as the larger amount of air can be stored in the form of air pockets, if the composite wetting state [22] is considered. Similarly, surface valleys with high R_{vk} values are capable of capturing air. Higher magnification SEM images (Fig. 2a–d, right) of the pp-HMDSO films revealed that they were composed of quasi-spherical nanoparticles with the size in the range of ∼24–53 nm. These nanoparticles are stacked together to form a network of branches suggesting that it is not a close-packing case [23] of dense assembly. It can be proposed that the intersection of these branches facilitates the formation of island-like morphological features, as deposition proceeds. The AFM and SEM analysis signify a dual-scale morphology of the pp-HMDSO film surface, which in turn suggests that composite wetting state should be considered for further analysis of the corresponding wetting properties.

Figure 3a–d shows water droplets deposited on pp-HMDSO film surface with the corresponding θ_s indicated, as well as AFM and reconstructed SEM topographical images filtered to display the surface micro- and nanostructures which fall into the R_{fs} (e.g.
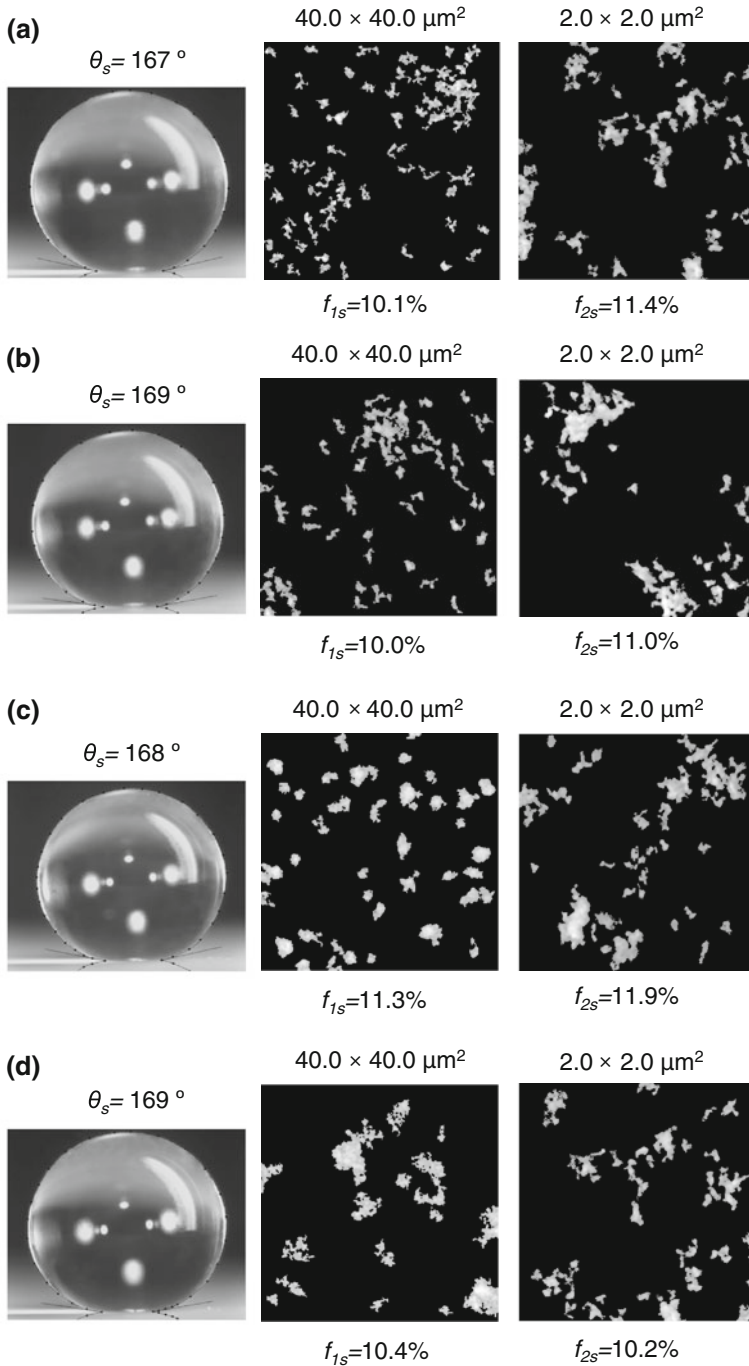
(a)

$\theta_s = 167\,°$

$40.0 \times 40.0\ \mu m^2$ $2.0 \times 2.0\ \mu m^2$

$f_{1s} = 10.1\%$ $f_{2s} = 11.4\%$

(b)

$\theta_s = 169\,°$

$40.0 \times 40.0\ \mu m^2$ $2.0 \times 2.0\ \mu m^2$

$f_{1s} = 10.0\%$ $f_{2s} = 11.0\%$

(c)

$\theta_s = 168\,°$

$40.0 \times 40.0\ \mu m^2$ $2.0 \times 2.0\ \mu m^2$

$f_{1s} = 11.3\%$ $f_{2s} = 11.9\%$

(d)

$\theta_s = 169\,°$

$40.0 \times 40.0\ \mu m^2$ $2.0 \times 2.0\ \mu m^2$

$f_{1s} = 10.4\%$ $f_{2s} = 10.2\%$

Fig. 3 *Left* water droplets on pp-HMDSO film surface with corresponding θ_s indicated as well as (*middle*) AFM and (*right*) reconstructed SEM topographical images filtered to display the surface micro- and nanostructures which fall into the R_{fs} region with f_{1s} and f_{2s} calculated. The pp-HMDSO deposition time of **a** 30 s, **b** 60 s, **c** 180 and **d** 300 s

Fig. 2a–d, middle) region, with f_{1s} and f_{2s} calculated and displayed. Nano-structured pp-HMDSO films showed very similar θ_s close to 170° even at short deposition time of 30 s. As shown in Fig. 3a–d, the superhydrophobic pp-HMDSO film surface has a relatively different spatial and size distribution of surface micro-structures which fall into the R_{fs} region for deposition time of 30, 60, 180 and 300 s, respectively. In contrast, similarities can be observed in morphology of the surface nanostructures. Importantly, relatively similar f_{1s} and f_{2s} values (Fig. 2a–d, middle and right) were calculated for the micro- and nanostructures obtained at different deposition times. The solid fraction was calculated to be f_s = 1.2, 1.1, 1.3 and 1.1 % for the corresponding deposition times. Further, θ_e values of 178.6, 178.8, 178.6 and 178.8° with CAH < 1° were calculated. One can see, that θ_e increases with θ_s and decreases with f_s. Additionally, CAH increases with f_s and decreases with θ_s. The results show that different spatial and size distribution of the surface micro-structures, which are in primary contact with the water droplet, has a negligible effect on the experimental θ_s values, as long as the surface morphology with the estimated f_{1s} value of 10–11.3 % is maintained. Specifically, variation of the surface peak height had no significant effect on the experimental θ_s values, which correlates well with Zhang et al. observation that the height of the peak does not affect the contact state of the droplet, as long as air, trapped between the surface structures, prevents the liquid from penetrating into the gaps [16]. Also, the morphology of the nanostructures and that on the micrometer scale plays very important role in the superhydrophobicity, as f_{2s} in our case significantly reduced the solid fraction (f_s) that was in contact with the water droplet. Further, experimental CAH_{exp} values in the range of 1.3°–2.2° were determined for pp-HMDSO film surface for the deposition times of 30, 60, 180 and 300 s, in a good agreement with the estimated CAH (< 1°).

Previous studies have also demonstrated that plasma polymerization can lead to the formation of nanoparticles. For instance, Teare et al. [24] reported that sequential short continuous wave bursts of 1H,1H,2H,2H-perfluorooctyl acrylate plasma have led to the formation of low surface energy (static CA > 160°) nanoparticles. The formation of nanoparticles was attributed to the rapid monomer replenishment and only few secondary reaction processes within the electrical discharge. A more detailed possible explanation of what is happening in the actual plasma which leads to the formation of observed quasi-spherical nanoparticles will be given latter in this paper.

Chemical and Functional Properties

Functional surface groups can be correlated with surface energy hence affecting hydrophobicity. FTIR measurements were carried out to study the structure–property relationships of the deposited pp-HMDSO films. Figure 4a, a_1 show reflectance FTIR spectra of the pp-HMDSO film deposited for 300 s and are presented in wavenumber ranges and full panoramic. The broad band between 3,200 and 3,700 cm^{-1} can be assigned to O–H stretching in Si–OH bonds [9]. The Bousquet et al. [25] reported that the presence of Si–OH bonds in SiO_x structures is consistent with the porous nature of the SiO_2-like film, which is in a good agreement with our surface morphology analysis. Moreover, the resulting pp-HMDSO films have a low concentration of silanol groups on the surface, which would otherwise negatively affect the non-wetting properties of the pp-HMDSO, as silanols are of hydrophilic nature [26]. Another O–H band located at 1,630 cm^{-1} is due to the bending mode of H_2O [27, 28], which is due to the residual H_2O adsorbed from the reaction chamber and trapped inside the valleys of the pp-HMDSO film. Specifically, silanol group electronic density becomes delocalized from the O–H bond to the
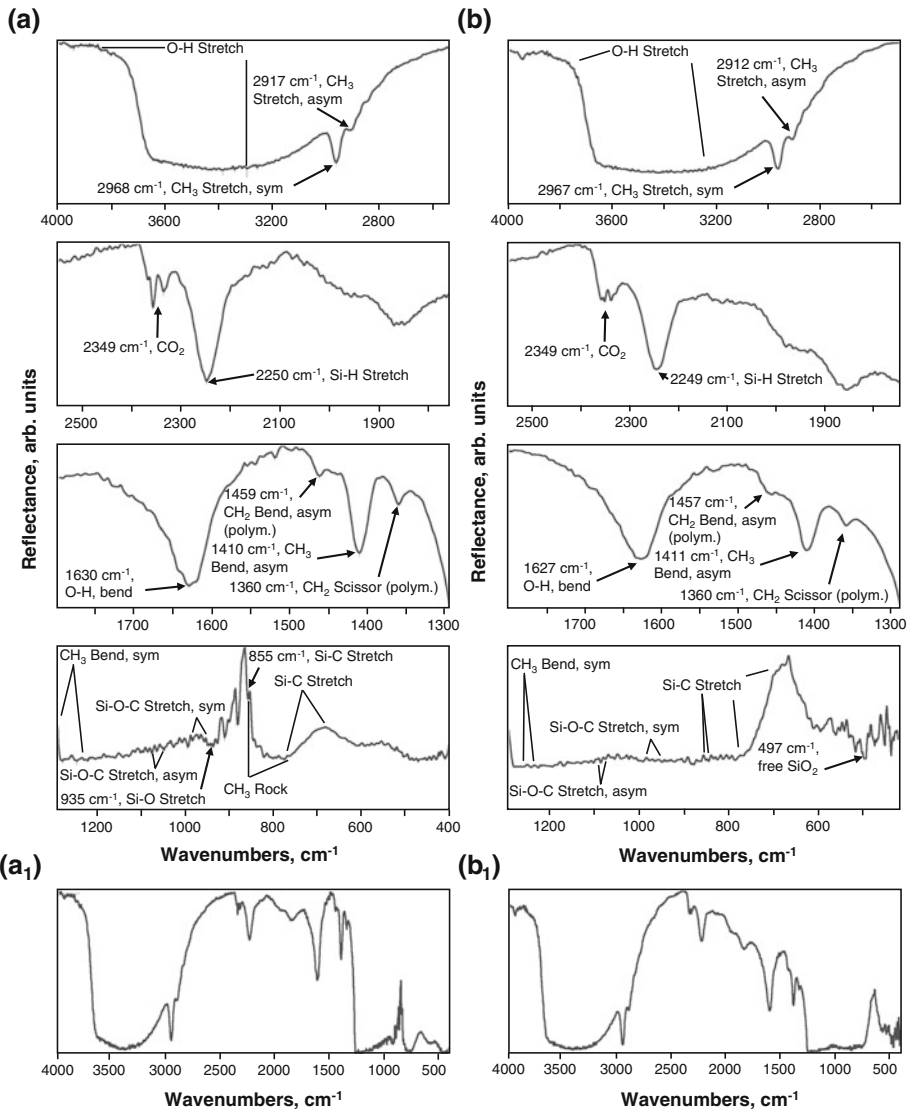
Fig. 4 Characteristic FTIR reflectance spectra of pp-HMDSO film for deposition time of **a**, **a₁** 300 s and **b**, **b₁** 30 s presented in wavenumber ranges with functional groups assigned and full panoramic

neighboring Si–O bond due to the donor–acceptor interaction, which makes it possible for the silanol groups to form strong hydrogen bonds with H_2O molecules [29]. This could additionally explain the presence of the 1,630 cm^{-1} peak. Furthermore, additional contributions to the 1,630 cm^{-1} peak could also appear due to the overlap with the C=C stretching vibration in the 1,610–1,650 cm^{-1} region [30]. The band assigned to Si–O stretching vibration that appears between 830 and 955 cm^{-1} corresponds to the strongly hydrogen-bonded Si–OH groups [31]. The doublet centered at 2,349 cm^{-1} is due to CO_2 [32]. Two distinct bands located at 1,360 and 1,459 cm^{-1} are assigned to the scissoring and

asymmetric bending vibrations of –CH_2 group corresponding to Si–CH_2–Si and Si–CH_2–CH_2–Si links [3, 33]. These links are assumed to play the most substantial role in the crosslinking [34] process during plasma polymerization of HMDSO. The presence of Si–CH_2–CH_2–Si links indicates good hydrothermal stability of pp-HMDSO film. 945–990 and 1,070–1,100 cm^{-1} peaks are due to the symmetric and asymmetric stretching vibrations of Si–O–C. Jing et al. reported [35] that the formation of Si–O–C ring links with CH_3 groups is responsible for the formation of nano-sized morphological features in the Si–OC composite film. Importantly, Spange et al. [36] reported that irreversible and, thus, stable linkage of the polymer to the surface is achieved through the formation of the covalent Si–O–C bonds and polymer networks on the surface. It could also be proposed that the inorganic SiO_x part of the pp-HMDSO fragment is linked with the organic part through Si–O–C chains. A very distinct band centered at 2,250 cm^{-1} is assigned to Si–H stretching vibrations, presumably in Si–O_2–SiH [11]. van der Steen et al. [37] have previously reported Si–H stretching vibration frequency at 2,250 cm^{-1}. Specifically, Delfino et al. [10] have shown that Si–H bonds terminate the outermost O_3–Si–O–Si–O_3 network of a thick $SiO_{x<2}$ film, thereby transforming what is normally a hydrophilic surface into one that is hydrophobic. It can be assumed that Si–H bonds play an important role in the formation of the nanoparticles observed in this work as they terminate the agglomeration of SiO_x during the deposition process of pp-HMDSO. Furthermore, Guermat et al. [8] reported that the replacement of Si–OH groups by the Si–H bonding groups results in a film densification. SEM presented in Fig. 2a–d, right, show porous pp-HMDSO structure, which is consistent with the presence of Si–OH and Si–H bonds in FTIR spectrum. Finally, bands at 750-770 cm^{-1} (Si–C stretching in Si–CH_3), 770-860 cm^{-1} (CH_3 rocking in Si–$(CH_3)_3$), 855 cm^{-1} (Si–C stretching in Si–$(CH_3)_3$), 1,240–1,290 cm^{-1} (CH_3 symmetric bending in Si–$(CH_3)_x$), 1,410 cm^{-1} (CH_3 asymmetric bending in Si–CH_3), 2,917 cm^{-1} (CH_3 asymmetric stretching) and 2,968 cm^{-1} (CH_3 symmetric stretching) indicate the presence of the methyl groups in the pp-HMDSO film [3, 11, 38]. Retention of the methyl groups present in the HDMSO monomer indicates a low surface free energy of pp-HMDSO and contributes to the superhydrophobic characteristics of the resultant films. Similar functional groups can be observed in the reflectance FTIR spectra of pp-HMDSO film deposited for 30 s presented in Fig. 4b, b_1. However, in 1,250–400 cm^{-1} region some differences are noticeable. Additional peak appearing at 497 cm^{-1} could be associated with the free SiO_2 [39], which provides further insights into the pp-HMDSO film formation mechanism.

pp-HMDSO Film Formation Mechanism

Figure 5 shows arc discharge generated HMDSO plasma between anode and cathode, displayed using thermal LUT scheme. Baeva et al. reported on two-temperature chemical non-equilibrium modelling of transferred arcs. It was demonstrated that the difference between the electron and heavy-particle temperatures in the arc fringes and the outer region is significant due to the low electron density and, correspondingly, the low collision frequency of electrons with heavy particles [40]. Based on these findings it can be proposed that regions a, b and c shown in Fig. 5 have considerably higher temperature and electron density, as compared with the regions d and h. It is considered that in regions a, b and c in Fig. 5, high monomer fragmentation of HMDSO occurs with the sufficient temperature and electron density to remove organic component of the starting monomer. Thus O/Si ratio can approach true SiO_2 value. Additionally, it can be overcome due to the formation of Si–OH functional groups. Consequently, in region d shown in Fig. 5 little HMDSO monomer

fragmentation occurs. It is purposed that region h in Fig. 5 acts as a stirring medium. Based on the experimental results presented here, a schematic of the possible pp-HMDSO film formation mechanism is proposed and shown in Fig. 6. Portion of HMDSO diffuses into the region ab (corresponds to a and b in Fig. 5) where SiO_2 nanoparticles are formed due to the high monomer fragmentation. Some of these particles are transferred to the region c where they undergo further agglomeration. The HMDSO monomer is subjected to little fragmentation in region d. The SiO_2 nanoparticles, agglomerated SiO_2 nanoparticles and HMDSO monomer fragments are mixed in the cooler region h. The SiO_2 nanoparticles and agglomerated SiO_2 nanoparticles are coated with HMDSO monomer fragments which contain methyl groups. Finally, pp-HMDSO film formation takes place, followed by the

Fig. 5 Arc discharge generated HMDSO plasma emission between anode and cathode displayed in the thermal LUT scheme with characteristic regions *a*, *b*, *c*, *d* and *h* assigned
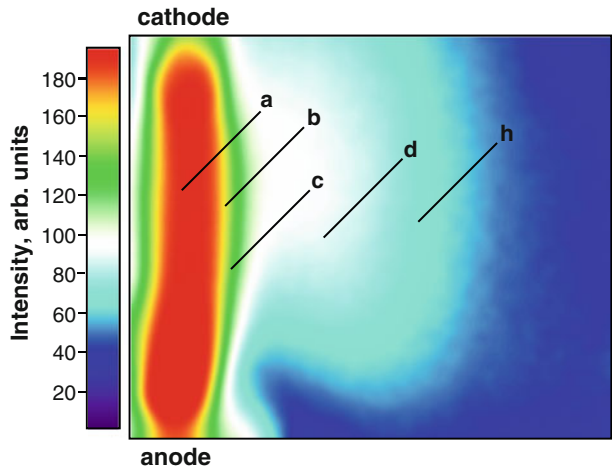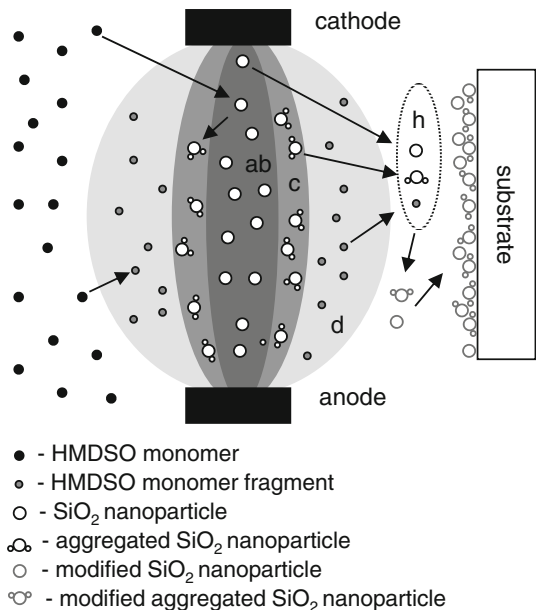

Fig. 6 Schematic of pp-HMDSO film formation mechanism

● - HMDSO monomer
• - HMDSO monomer fragment
○ - SiO₂ nanoparticle
⚬⚬ - aggregated SiO₂ nanoparticle
○ - modified SiO₂ nanoparticle
∿ - modified aggregated SiO₂ nanoparticle

nanoparticles impacting and adhering onto the substrate surface. As the deposition time increases, carbon from graphite electrodes and oxidized polymeric species may form Si–C functional groups, which are also transferred to substrate surface. The model presented in Fig. 6 is consistent with the behavior of observed pp-HMDSO surface morphological changes, non-wetting characteristics, chemical and functional properties.

Conclusions

This work has studied the surface morphology, structural, wetting and chemical properties of the pp-HMDSO films. These films were prepared using arc discharge with the deposition time varied from 30 to 300 s. As deposited, films were characterized using AFM, SEM, FTIR and CA measurements. AFM and SEM analysis showed dual-scale roughness of the films. The pp-HMDSO film was composed of the quasi-spherical nanoparticles stacked together to form a branched network. The intersection of these branches facilitated the formation of the island-like morphological features which grew in a three-dimensional manner and interconnected to form larger aggregates as the deposaition time increased. As the pp-HMDSO film grew, spiky surface morphology evolved into a bumpy one with the dual-scale roughness maintained. The deposited nano-structured pp-HMDSO films exhibited superhydrophobic properties with θ_s close to 170°, CAH_{exp} in the range of 1.3°–2.2°, θ_e approaching 180° and CAH < 1° even for short deposition time of 30 s. The Furthermore, different spatial and size distribution of surface micro-structures with f_{1s} in the range of 10–11.3 % had negligible effect on the experimental θ_s values. It was demonstrated, that the morphology of pp-HMDSO nanostructure features significantly reduced the solid fraction (f_s) that was in contact with a water droplet. The porous pp-HMDSO structure was consistent with the presence of Si–OH and Si–H groups in FTIR spectrum. The presence of the Si-CH$_2$–Si and Si–CH$_2$–CH$_2$-Si links in FTIR spectrum was consistent with the HMDSO polymerization proceeding during the arc discharge. It was proposed that the inorganic SiO$_x$ part of the pp-HMDSO fragment was linked with its organic part through the Si–O–C chains. Retention of the methyl groups in pp-HMDSO contributed to the superhydrophobic characteristics of the resultant film. The present work also suggests a mechanism for the pp-HMDSO film formation.

References

1. Lazauskas A, Grigaliunas V, Guobienė A, Puišo J, Prosyčevas I, Baltrusaitis J (2013) Polyvinylpyrrolidone surface modification with SiOx containing amorphous hydrogenated carbon (a-C:H/SiOx) and nitrogen-doped a-C:H/SiOx films using Hall-type closed drift ion beam source. Thin Solid Films 538:25–31
2. Lazauskas A, Grigaliūnas V, Meškinis Š, Kopustinskas V, Guobienė A, Gudonytė A, Andrulevičius M, Tamulevičius T (2009) Hydrophobic diamond like carbon film for surface micromachining. Mater Sci Medzg 15:196–200
3. Benıtez F, Martınez E, Esteve J (2000) Improvement of hardness in plasma polymerized hexamethyldisiloxane coatings by silica-like surface modification. Thin Solid Films 377:109–114
4. Miyachi H, Hiratsuka A, Ikebukuro K, Yano K, Muguruma H, Karube I (2000) Application of polymer embedded proteins to fabrication of DNA array. Biotechnol Bioeng 69:323–329

5. Puleo DA, Kissling RA, Sheu MS (2002) A technique to immobilize bioactive proteins, including bone morphogenetic protein-4 (BMP-4), on titanium alloy. Biomat 23:2079–2087
6. Kim SJ, Song E, Jo K, Yun T, Moon M-W, Lee K-R (2013) Composite oxygen-barrier coating on a polypropylene food container. Thin Solid Films 540:112–117
7. Radeva E (1997) Thin plasma-polymerized layers of hexamethyldisiloxane for acoustoelectronic humidity sensors. Sens Actuators B 44:275–278
8. Guermat N, Bellel A, Sahli S, Segui Y, Raynaud P (2009) Thin plasma-polymerized layers of hexamethyldisiloxane for humidity sensor development. Thin Solid Films 517:4455–4460
9. Aumaille K, Vallée C, Granier A, Goullet A, Gaboriau F, Turban G (2000) A comparative study of oxygen/organosilicon plasmas and thin SiOxCyHz films deposited in a helicon reactor. Thin Solid Films 359:188–196
10. Delfino M, Tsai W, Reynolds G, Day M (1993) Hydrogenating silicon dioxide in an electron cyclotron plasma. Appl Phys Lett 63:3426–3428
11. Grimoldi E, Zanini S, Siliprandi R, Riccardi C (2009) AFM and contact angle investigation of growth and structure of pp-HMDSO thin films. Eur Phys J D 54:165–172
12. Lazauskas A, Grigaliūnas V, Ecarla F, Caunii M (2012) A comparative evaluation of surface morphology, cohesive and adhesive properties of one-step and two-step thermal deposited chromium thin films on glass substrates. Appl Surf Sci 258:7633–7638
13. Sedláček M, Silva Vilhena LM, Podgornik B, Vižintin J (2011) Surface topography modelling for reduced friction. Stroj Vestn J Mech Eng 57:674–680
14. Stalder A, Kulik G, Sage D, Barbieri L, Hoffmann P (2006) A snake-based approach to accurate determination of both contact points and contact angles. Colloids Surf A 286:92–103
15. Chen W, Fadeev AY, Hsieh MC, Öner D, Youngblood J, McCarthy TJ (1999) Ultrahydrophobic and ultralyophobic surfaces: some comments and examples. Langmuir 15:3395–3399
16. Zhang H, Li W, Cui D, Hu Z, Xu L (2012) Design of lotus-simulating surfaces: thermodynamic analysis based on a new methodology. Colloids Surf A 413:314–327
17. Erbil HY, McHale G, Rowan S, Newton M (1999) Determination of the receding contact angle of sessile drops on polymer surfaces by evaporation. Langmuir 15:7378–7385
18. Pogorzelski SJ, Berezowski Z, Rochowski P, Szurkowski J (2012) A novel methodology based on contact angle hysteresis approach for surface changes monitoring in model PMMA-Corega Tabs system. Appl Surf Sci 258:3652–3658
19. Herminghaus S (2000) Roughness-induced non-wetting. Europhys Lett 52:165
20. Ohring M (2001) Materials science of thin films. Academic press, London
21. Gadelmawla ES, Koura MM, Maksoud TMA, Elewa IM, Soliman HH (2002) Roughness parameters. J Mater Process Technol 123:133–145
22. Malshe A, Rajurkar K, Samant A, Hansen HN, Bapat S, Jiang W (2013) Bio-inspired functional surfaces for advanced applications. CIRP Ann Manuf Technol 62:607–628
23. Genzer J, Efimenko K (2006) Recent developments in superhydrophobic surfaces and their relevance to marine fouling: a review. Biofouling 22:339–360
24. Teare D, Spanos C, Ridley P, Kinmond E, Roucoules V, Badyal J, Brewer S, Coulson S, Willis C (2002) Pulsed plasma deposition of super-hydrophobic nanospheres. Chem Mat 14:4566–4571
25. Bousquet A, Granier A, Goullet A, Landesman J (2006) Influence of plasma pulsing on the deposition kinetics and film structure in low pressure oxygen/hexamethyldisiloxane radiofrequency plasmas. Thin Solid Films 514:45–51
26. Tielens F, Gervais C, Lambert JF, Mauri F, Costa D (2008) Ab initio study of the hydroxylated surface of amorphous silica: a representative model. Chem Mat 20:3336–3344
27. Frost RL, Ding Z, Martens WN, Johnson TE, Kloprogge JT (2003) Molecular assembly in synthesised hydrotalcites of formula CuxZn6-xAl2 (OH) 16 (CO3). 4H2O-a vibrational spectroscopic study, spectrochim. Acta A 59:321–328
28. Martinez J, Ruiz F, Vorobiev YV, Pérez-Robles F, González-Hernández J (1998) Infrared spectroscopy analysis of the local atomic structure in silica prepared by sol-gel. J Chem Phys 109:7511
29. Zhuravlev L (2000) The surface chemistry of amorphous silica. Zhuravlev model. Colloids Surf A 173:1–38
30. Jelínek M, Zemek J, Trchova M, Vorlíček V, Lančok J, Tomov R, Šimečková M (2000) CNx films created by combined laser deposition and rf discharge: XPS, FTIR and Raman analysis. Thin Solid Films 366:69–76
31. Awazu K, Kawazoe H, Seki K (1992) Growth mechanisms of silica glasses using the liquid phase deposition (LPD). J Non-Cryst Solids 151:102–108
32. Guerrero-Pérez M, Herrera M, Malpartida I, Larrubia M, Alemany L (2006) Characterization and FT-IR study of nanostructured alumina-supported V-Mo-WO catalysts. Catal Today 118:360–365

33. C. Vivien, R. Mascart, C. Dupret, P. Dhamelincourt, L. Gengembre, P. Supiot, Plasma polymer coatings deposited from hexamethyldisilazane downstream a microwave nitrogen plasma jet
34. Wrobel A, Czeremuszkin G, Szymanowski H, Kowalski J (1990) Plasma polymerization of carbosilanes: tetramethylsilane as a model monomer for reactivity study of silylmethyl groups. Plasma Chem Plasma Process 10:277–289
35. Jing S-Y, Lee H-J, Choi CK (2002) Chemical bond structure on Si-OC composite films with a low dielectric constant deposited by using inductively coupled plasma chemical vapor deposition. J Korean Phys Soc 41:769–773
36. S. Spange, U. Eismann, S. Höhne, E. Langhammer (1998) Application of cationic polymerization to grafting and coating of silica particles. In: Macromolecular symposia, Wiley Online Library, pp. 223–236
37. van der Steen GHAM, van den Boom H (1977) Raman spectroscopic study of hydrogen-containing vitreous silica. J Non-Cryst Solids 23:279–286
38. Kong MJ, Lee SS, Lyubovitsky J, Bent SF (1996) Infrared spectroscopy of methyl groups on silicon. Chem Phys Lett 263:1–7
39. El-Zahhar A, El-Deen S, Sheha R (2013) Sorption of iron from phosphoric acid solution using polyacrylamide grafted activated carbon. J Environ Chem Eng 46:27–38
40. Baeva M, Kozakov R, Gorchakov S, Uhrlandt D (2012) Two-temperature chemically non-equilibrium modelling of transferred arcs. Plasma Sources Sci Technol 21:055027